CHALMERS
UNIVERSITY OF TECHNOLOGY

Exploring the High-Temperature Window of Operation for Organic Photovoltaics: A Combined Experimental and Simulations Study

ADVANCED FUNCTIONAL MATERIALS
www.afm-journal.de

Exploring the High-Temperature Window of Operation for Organic Photovoltaics: A Combined Experimental and Simulations Study

Asfaw Negash, Jeroen Hustings, Allyson Robert, Zewdneh Genene, Desalegn Yilma, Dieter Schreurs, Michiel Mathijs, Jori Liesenborgs, Frank Van Reeth, Koen Vandewal, Wendimagen Mammo, Shimelis Admassie, Wouter Maes, and Jean V. Manca**

The global climate change negatively affects the photovoltaic performance of traditional solar cell technologies. This article investigates the potential of organic photovoltaics (OPV) for high-temperature environments, ranging from urban hot summers (30—40 °C) and desert regions (65 °C) up to (aero) space conditions (130 °C), the thermal window in which OPV can operate. The approach is based on a combination of experiments and simulations up to 180 °C, moving significantly beyond the conventional temperature ranges reported in the literature. New 2*H*-benzo[*d*][1,2,3]triazole-5,6-dicarboxylic imide-based copolymers with decomposition onset temperatures above 340 °C are used for this study, in combination with non-fullerene acceptors. Contrary to their inorganic counterparts, OPV devices show a positive temperature coefficient up to ≈90 °C. At temperatures of 150 °C, they are still operational, retaining their room temperature efficiency. Complementary simulations are performed using an in-house developed software package that numerically solves the drift-diffusion equations to understand the general trends in the obtained current–voltage characteristics and the materials' intrinsic behavior as a function of temperature. The presented methodology of combined high-temperature experiments and simulations can be further applied to investigate the thermal window of operation for other OPV material systems, opening novel high-temperature application routes.

1. Introduction

Commercial solar cells are commonly used to power electrical appliances at mild temperatures.[1] In warm climates, where the sunlight is more intense, their performance decreases. Many regions in the world experience temperatures that can easily surpass 30 °C during local summer. Direct illumination onto the solar panels will increase the temperature even further. For example, organic photovoltaics (OPV) modules have been tested in Rwanda, where ambient temperatures range between 22 and 32 °C, displaying a large discrepancy between ambient and device temperature, as the back of the OPV module itself could heat up to 70 °C during the hottest part of the day.[2] Environments with extremely high temperatures range from deserts (≈65 °C) to photovoltaic concentrator applications (≈80 °C).[2–3]

For (aero) space applications, the European Space Agency (ESA) considers the temperature range from −175 to +130 °C.[4] Low orbital space flights are known to

A. Negash, J. Hustings, A. Robert, M. Mathijs, J. V. Manca
UHasselt
X-LAB
Agoralaan Building D, Diepenbeek B-3590, Belgium
E-mail: negasha@mpip-mainz.mpg.de; jean.manca@uhasselt.be

A. Negash
Max Planck Institute for Polymer Research
Ackermannweg 10, 55128 Mainz, Germany

A. Negash
Department of Chemistry
Debre Berhan University
P.O. BOX 445, Debre Berhan Ethiopia

Z. Genene
Department of Chemistry and Chemical Engineering
Chalmers University of Technology
Gothenburg SE-412 96, Sweden

D. Yilma, W. Mammo, S. Admassie
Department of Chemistry
Addis Ababa University
P.O. BOX 33658, Addis Ababa Ethiopia

D. Schreurs, K. Vandewal, W. Maes
UHasselt
IMO-IMOMEC
Wetenschapspark 1, Diepenbeek B-3590, Belgium

J. Liesenborgs, F. Van Reeth
UHasselt
Expertise Centre for Digital Media (EDM)
Diepenbeek B-3590, Belgium

The ORCID identification number(s) for the author(s) of this article can be found under https://doi.org/10.1002/adfm.202308666

DOI: 10.1002/adfm.202308666

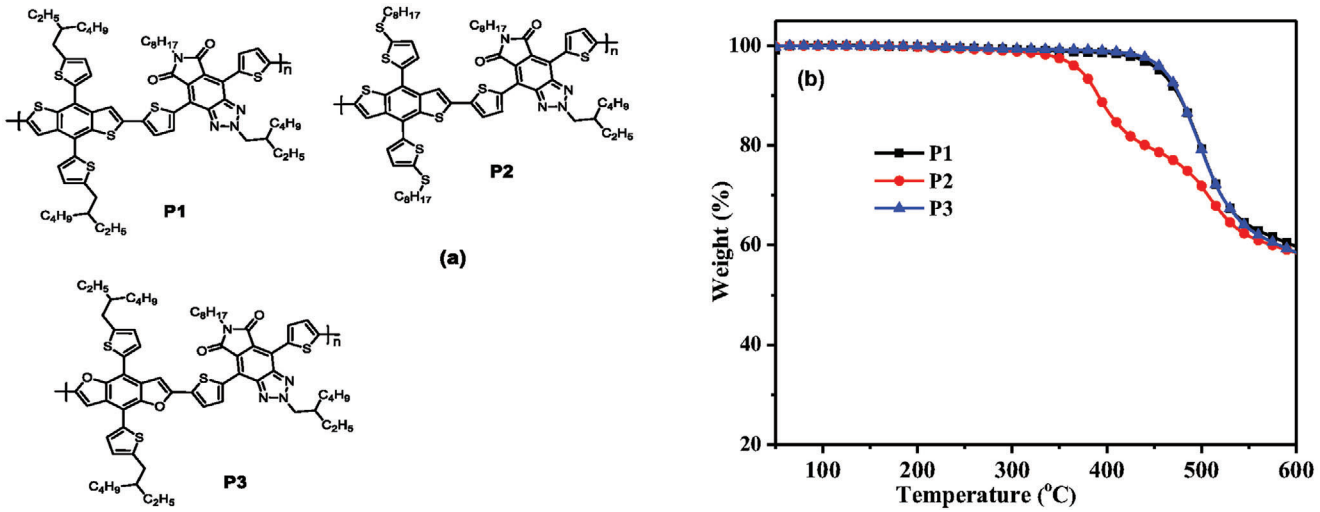

Figure 1. a) Chemical structures of polymers **P1**–**P3**. b) TGA plots for polymers **P1**–**P3** (determined at a heating rate of 20 K min^{-1} under N_2 atmosphere).

cycle between temperatures going from −100 °C in the Earth's shadow to +100 °C when directly exposed to sunlight.[5] An indication of the beneficial deployment of OPV technology in aerospace conditions is given by Kaltenbrunner et al.,[6] showcasing that organic-based technologies have a power-to-mass ratio (>30 W g^{-1}) which is orders of magnitude higher compared to inorganic alternatives. This could be a crucial factor in aerospace applications, where costs are mainly driven by weight. Earlier, we reported on in-flight tests performed during the stratospheric mission OSCAR in the framework of the ESA program BEXUS, which demonstrated for the first time organic-based solar cell operation in extraterrestrial conditions.[7] From this mission, it was clear that temperature has a crucial impact on photovoltaic performance. Further study of the temperature dependence of the intrinsic photovoltaic properties is, however, still needed. Evidently, space exhibits other extremes than a broad range of operating temperatures. Significant UV-radiation is present that might cause the decomposition of organics. This phenomenon is one of the leading causes of long-term degradation of OPV materials.[8] Other research demonstrated UV-induced deterioration of charge-transport layers and changes in micromorphology in the photoactive layer (PAL) of organic solar cells, both fullerene-based (PBTZT-stat-BDTT-8:PCBM)[9] and non-fullerene- based (PBDB-T-2Cl:IT-4F, and PM6:PY- OD:PY-OBO).[10] These effects can generally be mediated by applying UV-resistant layers, thereby substantially extending the device's lifetime.[11]

Additional information in the literature on the deployment and behavior of OPV technology in extreme environments or conditions is scarce. However, insights into the in situ temperature dependence of the operational behavior under less severe conditions have been reported.[12] The open-circuit voltage (V_{OC}) is temperature-dependent and decreases with increasing temperature. This trend is a consequence of the energy spread for charge carriers according to the Fermi–Dirac distribution and has been reported in the literature over a broad thermal window, encompassing values from 80 to 300 K.[13] In this temperature range, the short-circuit current density (J_{SC}) is known to exhibit a positive thermal coefficient, correlated to improved hopping of the free charge carriers when heating the device. Literature reports mention this trend for OPV devices based on pioneering model systems such as MDMO-PPV:$PC_{61}BM$,[14] P3HT:$PC_{61}BM$,[15] and PCPDTBT:$PC_{71}BM$.[16] These reports, however, are limited in scope as these observations are made within small temperature ranges between 25 and 80 °C. Lastly, the fill factor (FF) is known to slightly increase with temperature. Dyakonov et al.[13b] explained this phenomenon by an increased mobility that benefits the free charge carrier path length prior to recombination.

Temperature thus has a negative influence on the V_{OC} and a positive effect on the J_{SC} and FF, resulting in a maximum intrinsic performance temperature for each material combination. To the best of our knowledge, the previous high-temperature record for OPV was reported by Dunggu Lee et al. in 2020[17] for P3HT:$PC_{61}BM$ solar cells with metal oxide hole extraction layers investigated up to 147 °C. In this paper, we move beyond this record temperature and the conventional temperature ranges reported in the literature, by performing both in situ measurements and simulations of photovoltaic parameters as a function of temperature for OPV devices up to 180 °C to further explore the temperature frontiers and obtain more insights on the thermal window of operation for organic solar cells.

2. Results and Discussion

In this study, we use new 2*H*- benzo[*d*][1,2,3]triazole-5,6-dicarboxylic imide-based donor polymers, motivated by their elevated decomposition onset temperatures. Wei et al.[18] found that the position of heteroatoms and side chains can affect the photovoltaic properties of the polymers. However, the thermal window of operation of the OPVs has not yet been examined systematically in combination with the fullerene ($PC_{71}BM$) or (mostly) non-fullerene (ITIC) acceptors. Thus, these three new polymers are designed to study their impact on both the photovoltaic properties and explore the thermal window of operation for OPV devices.

Table 1. Molar masses, optical, electrochemical, and thermal properties of polymers **P1**–**P3**.

Polymer	M_n [kDa]	$Đ$	λ_{max} [nm]		E_g^{opt} [eV]	ε [g^{-1} L cm^{-1}]	HOMO [eV]	LUMO [eV]	T_d [°C]
			Solution	Film					
P1	57.0	3.9	550	608	1.83	65.3	−5.64	−3.37	458
P2	11.9	3.0	553	588	1.83	56.4	−5.60	−3.38	460
P3	14.9	5.2	615	635	1.79	62.9	−5.42	−3.36	359

In the following paragraphs, the polymer synthesis and characterization are provided, followed by their room temperature and temperature-dependent photovoltaic characteristics. To understand the general trends in the *J*–*V* characteristics and the materials' intrinsic behavior as a function of temperature, complementary simulations are performed using an in-house developed software package that numerically solves the drift-diffusion equations. The outcome of the combined experimental/simulations study on the temperature dependence of OPV performance is finally compared with other photovoltaic technologies.

2.1. Polymer Synthesis and Characterization

The chemical structures of the polymers used are shown in **Figure 1**a. The polymers were synthesized from the acceptor monomer 4,8-bis(5-bromothiophen-2-yl)−2-(2-ethylhexyl)−6-octyl-[1,2,3]triazolo[4,5-*f*]isoindole-5,7(2*H*,6*H*)-dione and benzo[1,2-*b*:4,5-*b*″]dithiophene (BDT, **P1** and **P2**)- and benzo[1,2-*b*:4,5-*b*″]difuran (BDF, **P3**)-based donor monomers by using the Stille polymerization reaction (see Supporting Information for details). The three polymers **P1**, **P2**, and **P3** are found to be soluble in chloroform, chlorobenzene, and *o*-dichlorobenzene. The molecular weights were determined by gel permeation chromatography (GPC) relative to polystyrene standards in 1,2,4-trichlorobenzene at a temperature of 135 °C (see Figure S2, Supporting Information, for chromatograms). The results are summarized in **Table 1**. The thermal properties of the polymers were evaluated by thermogravimetric analysis (TGA) and differential scanning calorimetry (DSC). All polymers exhibited good thermal stability, with decomposition onset temperatures (T_d) above 340 °C (Figure 1b and Table 1). Further analysis by DSC did not show any discernible transitions (i.e., no clear glass transition or melting behavior) between −90 and +320 °C, the upper limit of thermal stability. The observed thermal stability over a broad temperature range motivated us to use these materials in our pursuit of exploring the temperature window of operation for OPV.

The normalized UV–vis absorption spectra of **P1**–**P3** in dilute chloroform solutions and as thin films are shown in **Figure 2** and the corresponding optical parameters are summarized in Table 1. All copolymers showed similar absorption spectra in the wavelength region of 300–700 nm, with absorption maxima in chloroform solution at 550, 553, and 615 nm for **P1**, **P2**, and **P3**, respectively, all slightly red-shifted in film. The similar absorption of **P1** and **P2** in solutions may be due to having similar aggregation in solution. The red-shift (by 9 nm) of **P1** in the film presumably indicates increased conjugation length due to the high molecular weight of **P1** as compared to **P2** with low molecular weight. The red shift of **P1** in the film may be also due to the strong aggregation (highly ordered and densely packed state) of the **P1** than **P2**.[19] For **P3**, a red shift is observed compared to **P1** and **P2** due to the presence of the slightly stronger electron-donating character of the BDF chromophore.[20] The optical gaps (E_g^{opt}) for **P1**, **P2**, and **P3**, calculated from the absorption onsets of the thin film spectra, are 1.83, 1.83, and 1.79 eV, respectively. The molar absorption coefficients of **P1**, **P2**, and **P3** were determined to be 73.5, 56.4, and 62.9 g^{-1} L cm^{-1}, respectively. Importantly, the pristine polymers have complementary absorption with the acceptors ITIC and $PC_{71}BM$ (Figure 2b).

Cyclic voltammetry (CV) experiments were carried out to determine the HOMO and LUMO energy levels of **P1**–**P3** (**Figure 3**; Figure S3, Supporting Information). The oxidation onsets of **P1**, **P2**, and **P3** were determined to be 0.66, 0.62, and 0.44 V, and

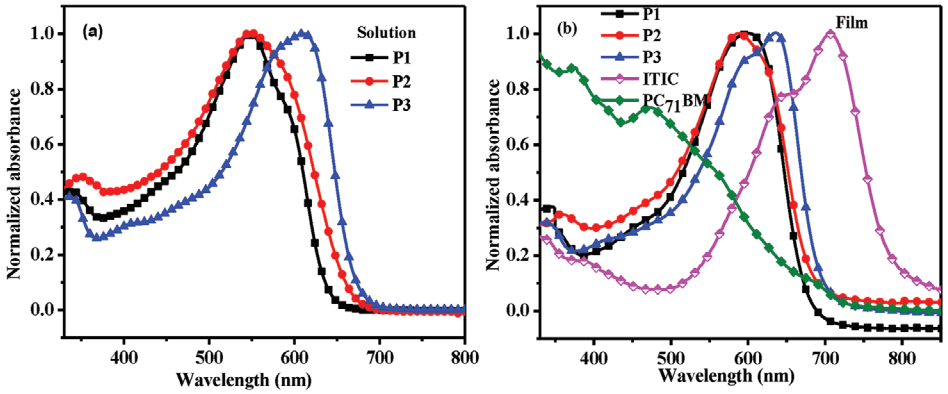

Figure 2. a) UV–vis absorption spectra for **P1**–**P3** in chloroform. b) UV–vis absorption spectra for thin films of the pristine polymers **P1**–**P3**, $PC_{71}BM$, and ITIC.

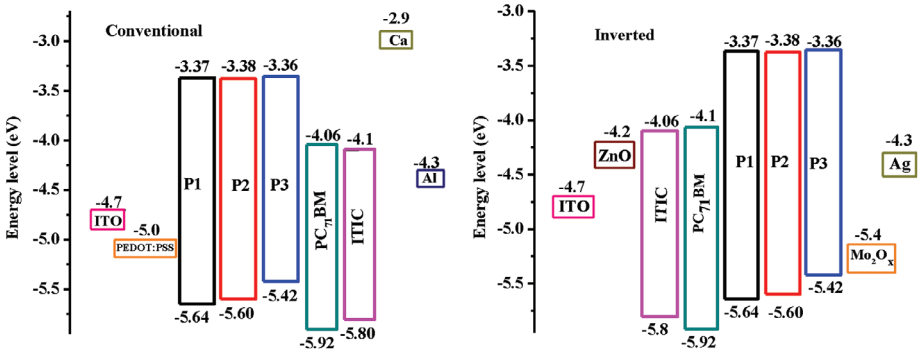

Figure 3. Energy levels for polymers **P1**–**P3** and acceptor materials $PC_{71}BM$ and ITIC, both for conventional and inverted devices.

the HOMO energy levels were calculated to be −5.64, −5.60, and −5.42 eV, respectively (Table 1). On the other hand, the reduction onsets were −1.61, −1.60, and −1.62 V and the corresponding LUMO energy levels were calculated to be −3.37, −3.38, and −3.36 eV, respectively (Table 1). The BDT-based polymers **P1** and **P2** have relatively deeper HOMO energy levels than **P3** due to the stronger electron-donating property of the BDF moiety.[21] This is expected to result in a higher V_{OC} in solar cell devices fabricated from **P1** and **P2** as compared to **P3**.

2.2. Room Temperature OPV Analysis

To evaluate the photovoltaic performances of the given polymers, both conventional (glass/ITO/PEDOT:PSS/polymer:ITIC/Ca/Al) and inverted devices (glass/ITO/ZnO/polymer:ITIC/Mo_2O_x/Ag) were fabricated. Optimizations of the **P1**–**P3**:ITIC weight ratios (Table S1, Supporting Information), film thicknesses, and solvent additives (Table S2, Supporting Information) were carried out. The optimized **P1**–**P3**:ITIC weight ratio was 1:1 for all the copolymers and the best results were achieved using chlorobenzene as a processing solvent and 0.2% of 1,8-diiodooctane (DIO) as a processing additive (see **Table 2**; Figure S4, Supporting Information). The as-cast **P1**:ITIC-based conventional solar cell devices afforded a power conversion efficiency (PCE) of 7.7%. The combined effect of the addition of 0.2% DIO and thermal annealing at 120 °C for 10 min resulted in an improved PCE of 8.3% with a (lower) V_{OC} of 0.84 V, an (improved) J_{SC} of 15.3 mA cm^{-2}, and an (improved) FF of 0.64 (Table 2; Figure S4, Supporting Information). On the other hand, the as-cast inverted solar cell

Table 2. Photovoltaic parameters for the optimized **P1**–**P3**:ITIC solar cells.

Polymer:ITIC	Additive	Thickness [nm]	V_{oc} [V]	J_{sc} [mA cm^{-2}]	$J_{sc,\,cal.}$ [a)] [mA cm^{-2}]	FF	PCE[b)] (average)[c)] [%]
P1:ITIC*	–	115 ± 3	0.86	14.59	13.99	0.611	7.67 (7.50 ± 0.12)
	0.2% DIO	113 ± 2	0.86	15.15	14.27	0.600	7.82 (7.75 ± 0.11)
	0.2% DIO/TA*	113 ± 2	0.84	15.28	14.71	0.642	8.28 (8.16 ± 0.10)
P1:$PC_{71}BM$*	–	108 ± 2	0.90	11.76	11.18	0.608	6.44 (6.16 ± 0.21)
	3%CN	106 ± 2	0.88	12.63	12.10	0.686	7.62 (7.47 ± 0.12)
P1:ITIC**	–	110 ± 3	0.84	15.12	14.08	0.59	7.51 (7.47 ± 0.12
	0.2% DIO	108 ± 4	0.86	15.41	14.58	0.617	8.17 (8.11 ± 0.13)
	0.2% DIO/TA*	108 ± 4	0.84	15.80	14.97	0.630	8.36 (8.26 ± 0.14)
P2:ITIC*	–	114 ± 3	0.86	13.12	12.70	0.449	5.27 (5.12 ± 0.13)
	0.2% DIO	115 ± 3	0.86	13.84	12.89	0.521	6.13 (6.00 ± 0.14)
	0.2% DIO/TA*	112 ± 2	0.86	13.48	13.10	0.551	6.39 (6.23 ± 0.15)
P2:ITIC**	–	120 ± 3	0.84	13.31	13.01	0.480	5.37 (5.29 ± 0.09)
	0.2% DIO	118 ± 2	0.84	13.38	13.20	0.500	5.63 (5.52 ± 0.12)
	0.2% DIO/TA*	116 ± 2	0.86	13.21	13.23	0.544	6.21 (6.15 ± 0.08)
P3:ITIC*	–	112 ± 2	0.80	14.01	13.30	0.571	6.70 (6.62 ± 0.11)
	0.2% DIO	109 ± 3	0.80	13.90	13.55	0.631	7.02 (6.87 ± 0.09)
	0.2% DIO/TA*	109 ± 3	0.78	13.57	13.51	0.624	6.60 (6.54 ± 0.12)
P3:ITIC**	–	115 ± 2	0.80	14.08	13.59	0.613	6.90 (6.84 ± 0.13)
	0.2% DIO	113 ± 3	0.82	13.88	13.77	0.667	7.59 (7.45 ± 0.12)
	0.2% DIO/TA*	113 ± 2	0.82	13.37	13.40	0.649	7.11 (7.08 ± 0.09)

* TA: thermal annealing at 120 °C for 10 min; [a)] J_{sc} calculated from the integrated EQE spectra. *Conventional device. **Inverted device; [b)] Maximum PCE; [c)] Average and standard deviations were calculated from more than 10 devices. DIO: 1,8-diiodooctane, CN: 1-chloronaphthalene.

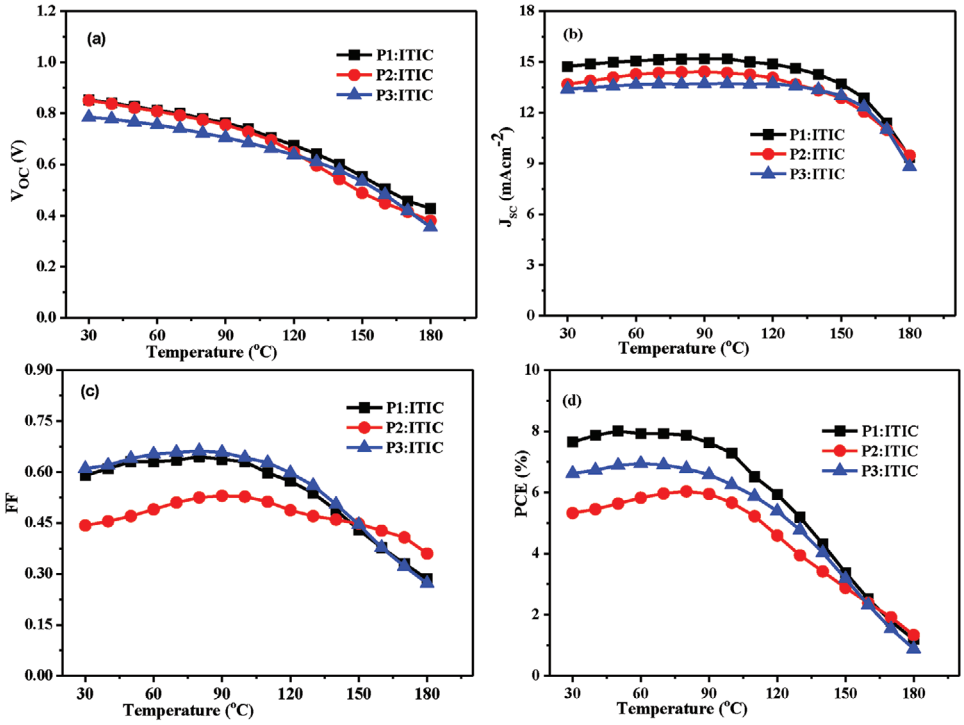

Figure 4. Variations of the photovoltaic output parameters with temperature for **P1**-**P3**:ITIC-based conventional solar cell devices: a) V_{OC}, b) J_{SC}, c) FF, and d) PCE.

devices afforded a PCE of 7.5%. Upon addition of 0.2% DIO and thermal annealing at 120 °C for 10 min, the PCE improved to 8.4% with an enhanced J_{SC} of 15.8 mA cm^{-2} and a FF to 0.63 (Table 2; Figure S5, Supporting Information). The **P2**:ITIC-based conventional devices achieved a best PCE of 6.4% with a V_{OC} of 0.86 V, a J_{SC} of 13.5 mA cm^{-2}, and a FF of 0.55. The PCE of the as-cast **P3**:ITIC-based conventional device was 6.7%. When adding 0.2% DIO, the PCE was improved to 7.0%. The combined effect of 0.2% DIO and thermal annealing at 120 °C for 10 min resulted in a drop in the PCE to 6.6% (Table 2; Figure S5c, Supporting Information). The performance of the inverted solar cell devices based on the **P3**:ITIC blend showed a similar trend. Thus, the PCE of the as-cast device was 6.9% and upon the addition of 0.2% DIO, the PCE improved to 7.6%. However, adding 0.2% DIO and thermal annealing at 120 °C led to a decrease in the PCE to 7.1%. Compared with the $PC_{71}BM$-based conventional devices, the **P1**:ITIC-based devices exhibited better PCEs, mainly due to the complementary absorption of **P1** and ITIC (see Figure 2b). The external quantum efficiency (EQE) was determined for the best conventional and inverted solar cell devices to evaluate the spectral responses and the accuracies of the photocurrents extracted from the solar cells. The maximum EQE values were ≈64–72% (Figure S4, Supporting Information). The current densities calculated by integrating the EQE spectra with the AM 1.5 G solar spectrum agree with the corresponding J_{SC} values determined from the *J*–*V* curves with a mismatch of less than 7% (Table 2).

In order to investigate the film morphologies of the photoactive layers, AFM measurements were carried out for the best-performing solar cell devices prepared without and with the combined effect of a processing additive (0.2% DIO) and thermal annealing (Figure S6, Supporting Information). Furthermore, photoluminescence (PL) quenching experiments were carried out to investigate the exciton dissociation and charge transfer behavior of the **P1**–**P3**:ITIC blends. The results indicate that effective electron transfer occurred from the donor copolymers to the ITIC acceptor, for the excitons generated in the donor phase (Figure S7, Supporting Information). The hole (μ_h) and electron (μ_e) mobilities of the OPV devices were investigated using the space charge limited current (SCLC) method. Higher charge carrier mobility and well-balanced μ_h/μ_e values were in line with the J_{SC}, FF, and photovoltaic performance (see Table 2; Table S3 and Figure S8, Supporting Information).

2.3. Temperature-Dependent OPV Analysis

To investigate the effect of temperature on the photovoltaic properties of the **P1**-**P3**:ITIC solar cells, experiments were performed on devices with conventional architecture fabricated using chlorobenzene as a processing solvent with 0.2% DIO. Thermal annealing was performed at 120 °C for 10 min, since these devices in general yielded the highest room temperature photovoltaic output.

Figure 4 shows the variations of the photovoltaic parameters (V_{OC}, J_{SC}, FF, and PCE) for **P1**:ITIC, **P2**:ITIC, and **P3**:ITIC-based conventional solar cell devices during the first heating step from room temperature to 180 °C. The generic trend observed for the various parameters as a function of temperature is similar for all investigated materials systems. With increasing temperature,

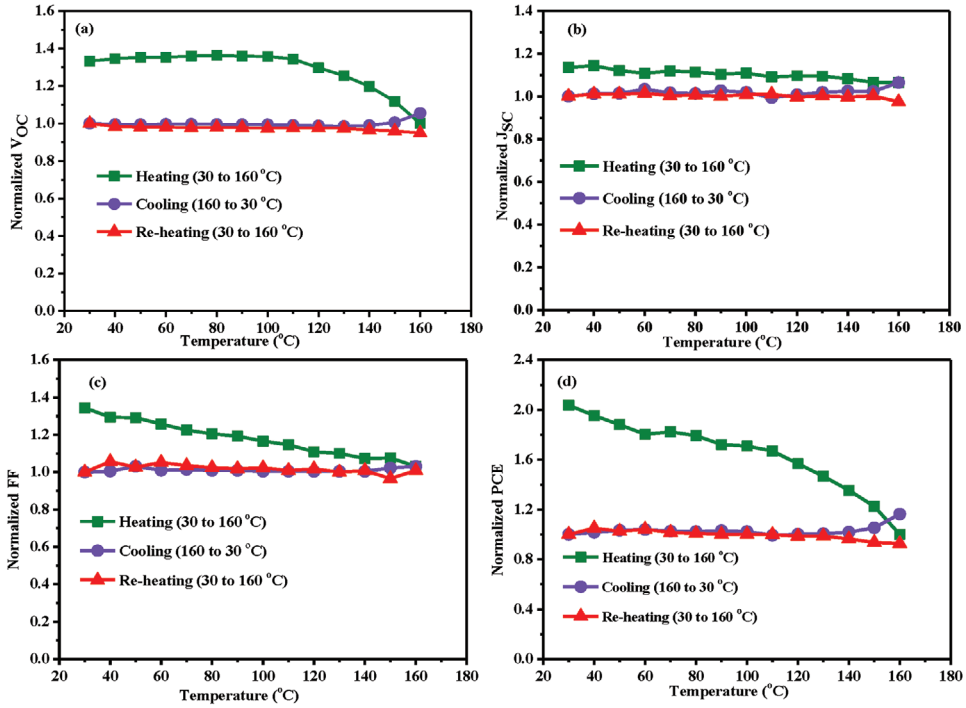

Figure 5. Variations of the normalized photovoltaic parameters (relative to the room temperature values of the second heating step) for conventional **P1**:ITIC solar cell devices upon performing a heating (30–160 °C) – cooling (160–30 °C) – re-heating (30–160 °C) cycle: a) V_{OC}, b) J_{SC}, c) FF, and d) PCE.

J_{SC}, FF, and PCE showed a bell-like curve consisting of an initial increase, followed by a decrease, while the V_{OC} showed a continuous decrease for all material combinations. The V_{OC} of the **P1-**, **P2-**, and **P3**-based devices decreases continuously as a function of increasing temperature from its initial value of 0.85, 0.84, and 0.79 V at 30 °C to 0.43, 0.38, and 0.36 V at 180 °C, respectively. The J_{SC} showed little variation in the given temperature range, with a slight linear increase from 30 to 150 °C, followed by a decrease between 150 and 180 °C. Upon in situ thermal heating of the **P1**:ITIC-based device, the FF improved from 0.59 at 30 °C to 0.65 at 80 °C and reduced to 0.29 at 180 °C. In situ thermal heating of the **P2**:ITIC-based device resulted in an improvement of the FF from 0.44 at room temperature to 0.53 at 90 °C, followed by a subsequent decrease. Likewise, the **P3**:ITIC-based device showed an enhanced FF from 0.61 at 30 °C to 0.66 at 90 °C and this dropped to 0.27 at 170 °C.

Furthermore, for the purpose of comparison, we also investigated the temperature dependence of the **P1**:$PC_{71}BM$ device parameters, which showed a similar trend to the **P1**:ITIC-based devices during the short interval (45 min measurement time) of the in situ heating experiment (Figure S9, Supporting Information). The initially observed slight increase in J_{SC} and the significant improvement in FF for all devices during the first linear heating step resulted in an initial increase of the PCE up to 80–90 °C. However, at temperatures above 100 °C, PCEs decreased in all cases because of the decline in V_{OC} and FF.[22] During the in situ heating experiment up to 180 °C, both types of devices (i.e., non-fullerene and fullerene) had stable active layer morphologies as observed from atomic force microscopy (AFM) and transmission electron microscopy (TEM) images (Figures S10 and S11, Supporting Information).

In order to investigate whether the observed behavior of the photovoltaic parameters as a function of temperature is reversible, subsequent heating and cooling steps were performed. For the sake of simplicity, in the following, we only focus on **P1**:ITIC-based devices, since these show similar temperature-induced behavior of the solar cell output parameters as the other material systems, and furthermore, the **P1**:ITIC devices gave the highest PCE.

The applied heating/cooling cycle consists of the following steps: heating (30 to 160°C), cooling (160—30 °C), and re-heating (30—160 °C). Here, a maximum temperature of 160 °C instead of 180 °C is chosen, since demonstrated in Figures S10 and S11 (Supporting Information) prolonged heating at 180 °C can yield thermally induced changes of the morphology. The evolution of the normalized photovoltaic output characteristics (normalized with the room temperature value at the start of the second heating step as a reference) for **P1**:ITIC during these subsequent thermal steps is shown in **Figure 5**. From this figure, it is clear that the characteristics observed during the first heating step differ from the ones obtained for the first cooling and second heating, which in general coincide, thus indicating a reversible behavior after the first heating step. This also indicates that during the first heating step, an initial irreversible effect takes place, of unknown nature. This irreversible drop in performance might be attributed to top electrode interface degradation.[23] Due to the coinciding curves of the photovoltaic parameters for the first cooling and second reheating step, the temperature range from room temperature to 160 °C can be considered as a reversible temperature window of operation for the **P1**:ITIC solar cells. To understand the observed trends of the photovoltaic parameters as a function of temperature in this reversible temperature range, the experimental data

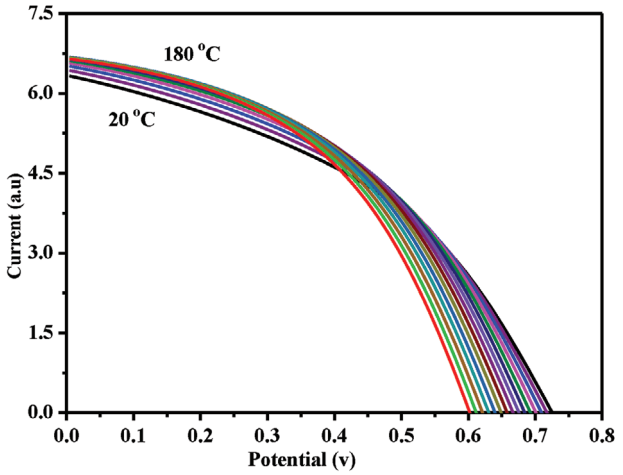

Figure 6. Evolution of the *J–V* curves for **P1**:ITIC solar cell devices in relation to temperature, calculated using *Simiconductor*.

are compared with the trends obtained from drift-diffusion simulations as described below.

2.4. Drift-Diffusion Simulations

Complementary to the presented temperature-dependent OPV characterization experiments, simulations are performed using an in-house developed software package called *Simiconductor* that numerically solves the drift-diffusion equations[24] (see Supporting Information and Experimental Section) to understand the general trends in the obtained current-voltage characteristics and the materials' intrinsic behavior as a function of temperature. *Simiconductor* aims to simulate the general behavior of bulk heterojunction (BHJ) OPV devices using the simplified MIM-model,[24] which approaches a BHJ as a metal-insulator-metal interface due to the similarity with the BHJ OPV architecture of a mixed donor-acceptor film sandwiched between two electrodes. *Simiconductor* is able to simulate junctions in 1D and 2D and is used here to conduct a 1D simulation for **P1**:ITIC devices in the thermal window from +20 to 180 °C. For each temperature interval of 10 °C, *J–V* curves were calculated from which the photovoltaic output parameters were extracted. Due to the simplicity of the device model used in *Simiconductor*, we use it to only draw qualitative conclusions, not quantitative ones, with an exception for the V_{OC}. The photovoltaic performance parameters were normalized at 30 °C to compare the results to experimental data. The *J–V* curves obtained by *Simiconductor* are displayed in **Figure 6**.

The linear behavior of the V_{OC} is well understood from the literature.[25] Its value increases steadily at colder temperatures and reaches a limit of 0.8 V, corresponding to the built-in voltage. The J_{SC} displays an initial linear increase with rising temperature before saturation sets in between 50 and 180 °C. This increase is related to the temperature dependence of the charge-carrier mobility. The opposite trend between V_{OC} and J_{SC} results in a trade-off that translates to a global maximum for efficiency at ≈70 °C.

Figure 7 shows the experimentally obtained *J–V* characteristics for a **P1**:ITIC conventional device together with the results from *Simiconductor*. The experimental data comprise the second heating cycle (30–160 °C), thereby reducing any annealing effects that might otherwise occur during the first heating. The data was once again normalized to 30 °C for quantitative analysis of the V_{OC}, J_{SC}, FF, and PCE. Although no exact match was obtained between both datasets, the similarities in the thermal evolutions are striking, given the simplicity of the model employed by *Simiconductor*. We obtain similar trends for the experimental and simulated values. Figure 7 additionally shows how the FF evolves as a function of temperature. Although the experimental and simulated values for the FF do not numerically correspond, of particular relevance here is that the global trend is similar, i.e., an initial increase of the FF from room temperature up to ≈130 °C, followed by a decrease with further increasing temperatures. Since the FF is determined by the competition between the extraction of free charges and recombination, the initial increase can be due to the temperature-induced improved charge transport, while at higher temperatures recombination becomes more dominant.[26]

In conclusion, the overall similar trends of the experimental and simulated values suggest that drift-diffusion simulations are a useful tool to better understand the generic trends of intricate dynamics and the effect of temperature on the photovoltaic parameters of organic solar cells, and confirm their potential high-temperature window of operation.

2.5. OPV versus Other Solar Cell Technologies

The combined experimental simulation results presented above indicate that OPV is an interesting photovoltaic technology for high-temperature environments. Contrary to inorganic counterparts and other emerging PV classes such as dye-sensitized cells (DSSCs) and perovskite solar cells (PSC), the studied OPV devices show a positive temperature coefficient up to ≈90 °C. At temperatures of 150 °C, they are still operational, retaining their room temperature efficiency.

In the following, we aim to compare the temperature dependence of the photovoltaic performance of **P1**:ITIC, and OPV devices in general, to that of different PV technologies: on the one hand, common inorganic PV technologies: monocrystalline Si, polycrystalline Si, copper indium gallium selenide (CIGS), and a heterostructure with intrinsic thin layer (HIT),[27] and on the other, emerging PV classes such as dye-sensitized cells (DSSCs) and perovskite cells. The former types of devices are known to exhibit a negative temperature coefficient for performance, as reported by Paudyal et al.[27] for the temperature range from −10 to +70 °C and tabulated in **Table 3**. Negative temperature coefficients have also been reported for the mentioned emergent types of devices (i.e., DSSCs and PSCs).[28] Dong et al.[29] have demonstrated perovskite solar cells operating at 200 °C, based on inorganic $CsPbI_2Br$ perovskite and carbon nanotubes as hole extraction electrodes, and compared their high-temperature behavior with other PV technologies. Raga et al. measured the power conversion efficiency for N719 stained TiO_2 DSSCs at temperatures ranging from −7 to 70 °C. They note a maximum efficiency ≈30—40 °C before a significant drop off. From their data, a negative temperature coefficient of −0.29%/°C can be computed for the highest reported temperature of 70 °C.[30] These negative temperature coefficients for the performance of the perovskite

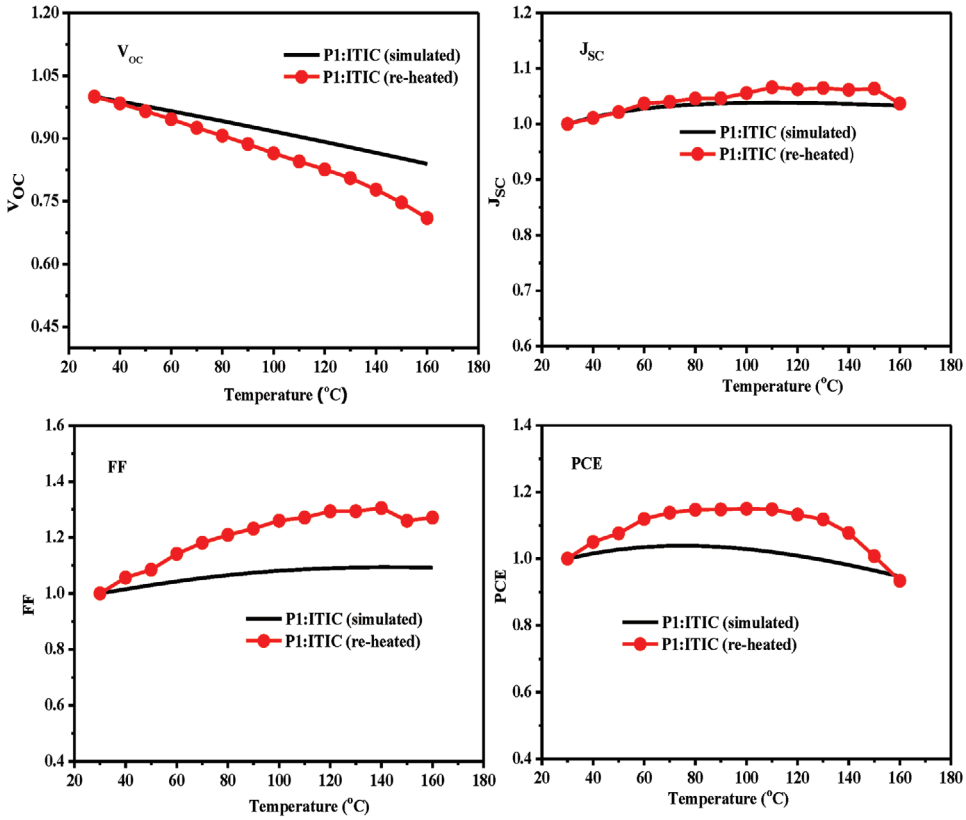

Figure 7. Evolution of the *J–V* characteristics for a **P1**:ITIC device in relation to temperature: simulated data plotted against experimentally obtained data. The data are normalized at 30 °C for the second heating step.

solar cells and DSSCs reported by Dong et al. and Raga et al., are tabulated in Table 3 alongside our P1:ITIC results and other PV technologies from Paudyal et al.[27]

Figure 8 shows the corresponding relative change in PCE as a function of temperature compared to room temperature values for various PV technologies, illustrating the opposing effects of the difference in temperature coefficients between OPV and other PV technologies. While the various classes of solar cells show a linear decrease in performance for increasing temperature, **P1**:ITIC displays a relative increase of up to 15% ≈100 °C. After attaining a maximum plateau region ≈100 °C, the PCE of **P1**:ITIC decreases at higher temperatures. Since PCE is proportional to the product of J_{SC}, V_{OC}, and FF, the displayed bell-shaped PCE graph of **P1**:ITIC in Figure 8 can be explained by the temperature dependence of these photovoltaic parameters as shown in Figure 7: the raising part of the PCE graph can be ascribed to the dominating contribution of the increasing FF and J_{SC}, while the

Table 3. Temperature coefficient for efficiency around standard test conditions of 25 °C, given for different PV technologies.[27–28,30]

PV technology	CT (PCE) [%/°C]	Reported efficiency at 25 °C [%]
Mono c-Si	−0.30	19
Poly c-Si	−0.34	16.6
CIGS	−0.26	12.6
HIT	−0.22	19.4
PSC	−0.035	5.413
DSSC	−0.29	4.95
P1:ITIC*	0.49	3.94

P1:ITIC*-Second heating OPV.

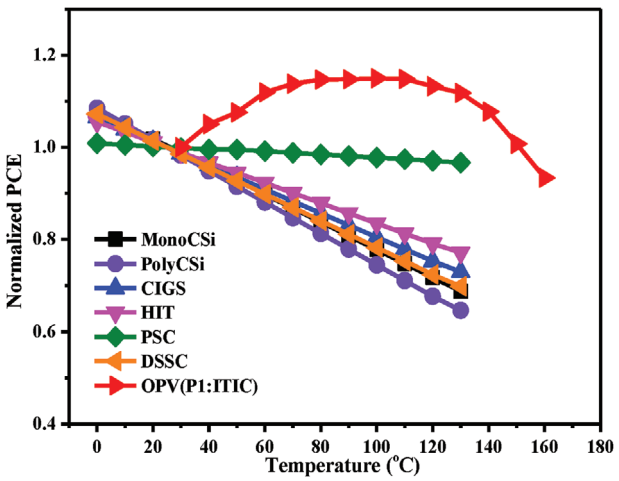

Figure 8. Temperature dependence PCE of **P1**:ITIC (relative to the room temperature values of the second heating step) OPV compared to different inorganic technologies, DSSCs, and perovskite solar cells (as extrapolated from their temperature coefficients in Table 3).

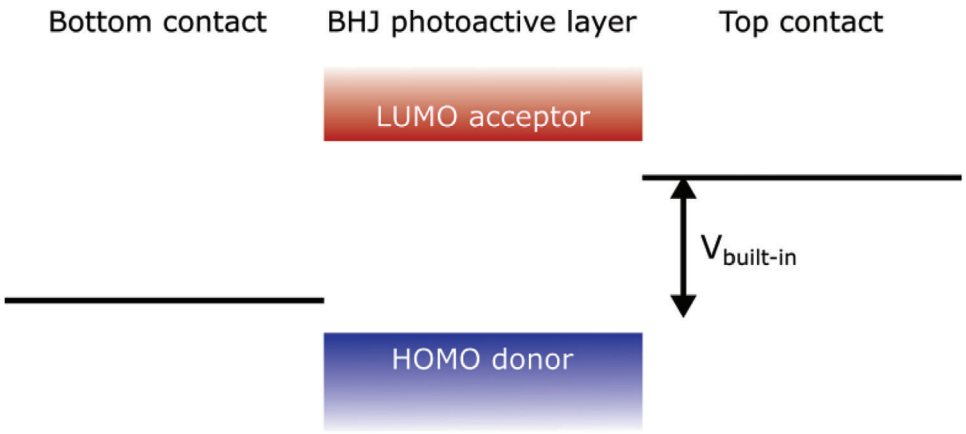

Figure 9. Representation of a BHJ OPV device based on the MIM model. On each side of the device, there is a metal contact with specified work functions. In between resides the photoactive layer with effective HOMO and LUMO levels.

decreasing part at higher temperatures is due to the dominating contribution of the decreasing V_{OC}.

For a proper comparison of the high-temperature performance of the various photovoltaic technologies, however, the crucial figure of merit is the absolute PCE at a given temperature. Although in the context of high-temperature photovoltaics, **P1**:ITIC has an interesting temperature coefficient compared to the other tabulated PV technologies, its room temperature efficiency is significantly lower (see Table 3). However, as the best research-cell efficiency for OPV has currently reached 19.2%,[31] there is plenty of room for improvement, and future high-temperature studies involving more performant OPV material systems are needed to draw realistic conclusions on the competitive potential of OPV for high-temperature applications.

3. Conclusions

In this work, we explored the high-temperature window of operation for organic solar cells. In situ analysis of the temperature window of operation for OPV devices using a combined experimental and simulations study was performed over a sizeable thermal window from 30 to 180 °C. 2*H*- Benzo[*d*][1,2,3]triazole-5,6-dicarboxylic imide-based copolymers were used for this study due to their good thermal stability and decomposition onset temperatures above 340 °C, in combination with both a fullerene ($PC_{71}BM$) and non-fullerene (ITIC) acceptors. The studied devices showed a positive temperature coefficient up to ≈90 °C and they were still operational in the investigated high-temperature window of operation-beyond the previously reported high-temperature OPV record of 147 °C, while retaining their room temperature efficiency at 150 °C. Complementary simulations using the in-house developed software package *semiconductor*-which numerically solves the drift-diffusion equations were introduced to interpret the obtained current-voltage characteristics and the materials' intrinsic behavior as a function of temperature. Although no exact numerical match was obtained between the experimental and simulated datasets for the V_{OC}, J_{SC}, FF, and PCE as a function of temperature, the overall general trends observed in experiments and simulations are strikingly similar. The proposed drift-diffusion simulations are thus a useful tool to understand the generic trends of intricate dynamics and the effect of temperature on the photovoltaic parameters of organic solar cells and confirm the potential high-temperature window of operation for OPV.

A key observation is that the devices in this study display a reverse effect of temperature on their performance compared to other PV technology, by performing relatively better at elevated temperatures, suggesting that OPV devices might potentially have competitive benefits in hot environments. This behavior is observed in both experiments and simulations and is among others attributed to the intrinsic temperature dependence of the charge-carrier mobility of organic materials.

To further explore the high-temperature window of operation for OPV and a more direct assessment of its competitive high-temperature potential compared to other classes of photovoltaic devices, it is recommended for follow-up investigations that the proposed measurement/simulation methodology will be applied to other, especially more performant, OPV material systems (e.g., PM6:BTP-eC9,[32] and PM6:Y6[33]) together with complementary long-term aging studies.

In the development toward high-temperature OPV, it has to be emphasized that in the aimed temperature window of operation no degradation sets in. The high-temperature limit of the temperature window of operation will therefore be determined by material properties such as glass transition and decomposition temperatures, which can serve as a guideline for materials synthesis. In relation to the latter, caution should be taken concerning the

Table 4. Intrinsic OPV parameters that are affected by temperature and their corresponding expressions.

Temperature-dependent variable	Expression
Diffusion coefficient	$D(T) = \mu kT/q$
Charge-carrier mobility[36]	$\mu(T) = \mu_o e^{E_A/kT}$
Effective density of states of conduction/valence band[37]	$N_{c/v}(T) \approx T^{3/2}$
Charge-carrier number density[37]	$n_i(T) = \frac{v}{N_c N_v} e^{-(\text{HOMO}-\text{LUMO})/kT}$

long-term stability of the device's performance and morphology at elevated temperatures, a subject requiring dedicated in-depth research. Although the proposed methodology is valuable as a rapid initial screening to explore the thermal window of operation of OPV, it is however not sufficient for predicting quantitatively lifetimes at elevated temperatures. Information in the literature on the deployment and long-term behavior of OPV technology in extreme environments or conditions is scarce. Most of the thermal studies reported using ISOS test Protocols.[34] These latter are established, consensus test protocols for life test models to predict the long-term reliability and lifetime of organic solar cells in typical operation conditions on Earth. The highest test temperature in the current ISOS test protocols therefore amounts to 85 °C. Toward a quantitative prediction of the long-term operation of OPV at more extreme high temperatures (e.g., aerospace applications), novel, appropriate ISOS-like test protocols need to be developed, beyond the current highest ISOS test temperature of 85 °C.

The presented insights and methodology of high-temperature experiments/simulations related to the high-temperature window of operation of OPV in combination with performant and thermally robust OPV materials can open novel high-temperature application routes on Earth and in space.

4. Experimental Section

Temperature-Dependent Current–Voltage Measurements: An in-house hybrid heating/measurement setup was developed, allowing in situ current—voltage (*I–V*) measurements under illumination on a 2.5 × 2.5 cm^2 substrate while heated. This setup allowed for measurements in the temperature range between 30 and 200 °C (Figure S1, Supporting Information). The temperature was manually controlled with temperature intervals of 10 °C, with a short initial time period for the device to stabilize at the specified temperature.

Drift-Diffusion Simulations: The in-house developed software *simiconductor* aimed to simulate the general behavior of bulk heterojunction (BHJ) OPV devices using the simplified MIM model, which approached a BHJ as a metal-insulator-metal interface. This approach limited the ability to simulate in detail the photovoltaic output characteristics of specific devices, but still represented a good picture of the generic occurring mechanisms. A visual representation of this approach is given in **Figure 9**, where the intrinsic layer represented the PAL with a valence band equal to the highest occupied molecular orbital (HOMO) energy level of the donor material and a conduction band equal to the lowest unoccupied molecular orbital (LUMO) energy level of the acceptor material. This layer was sandwiched between two metallic contacts. The difference in work functions between the top and bottom contact was representative of a built-in voltage V_{bi}. An excitation in the middle layer corresponded to a successfully charge-separated exciton in the PAL of the OPV device. The mechanism of drift-diffusion subsequently described the transport of the free charge carriers to the corresponding contacts. A further description of the MIM model and the drift-diffusion equations were given in a recent review paper on the modeling of organic solar cells by Li et al.[24] *Simiconductor* was able to simulate junctions in 1D and 2D, but this work was restricted to 1D simulations. The software was developed by Jori Liesenborgs and is available for download at research at https://research.edm.uhasselt.be/simiconductor/web/pn.hl.[35] Further information on *Simiconductor* is available at this link and in Supporting Information. The temperature-dependent parameters are summarized in **Table 4**.

These parameters were temperature-dependent directly and the expressions had been taken from the literature, with *k* the Boltzmann constant and E_A the hopping activation energy. The charge-carrier number density was only used in the calculation of the recombination parameter, which in the sets of simulations also depends on temperature, due to it being a function of the charge-carrier mobility and the charge-carrier number density. The recombination parameter in the table below (**Table 5**) used the bimolecular recombination model, whose expression contained the Langevin prefactor.[35]

Table 5. Material properties and their assigned values for a **P1**:ITIC-based organic solar cell as requested by *Simiconductor*.

Parameter	Value
PAL thickness [m]	1.15×10^{-7}
Recombination parameter	0.01
Cathode work function [eV]	4.2
Anode work function [eV]	5
Molar absorption coefficient [g^{-1} Lcm^{-1}]	65.3
Generation rate [m^{-3} s^{-1}]	1.00×10^{-29}
Effective density of states (DoS) at T_r* [m^{-3}]	5.00×10^{26}
DoS width [eV]	0.09
Hole mobility at T_r [m^2 V^{-1} s^{-1}]	6.79×10^{-8}
Electron mobility at T_r [m^2 V^{-1} s^{-1}]	3.04×10^{-8}
Relative permittivity	4.5

*T_r: room temperature.

The simulations were based on the material properties of the **P1**:ITIC BHJ system described in Tables S1–S3 (Supporting Information). The parameters requested by *Simiconductor* are summarized in Table 5. Many of these values were obtained from experimental data, taken either from this work or previous work.[38] Other values had to be estimated. The generation rate was derived from the experimentally measured molar extinction coefficient.

Supporting Information

Supporting Information is available from the Wiley Online Library or from the author.

Acknowledgements

A.N. gratefully acknowledges BOF Bilateral Scientific Cooperation funding from Hasselt University, Belgium (BOF2021-R11935) and the Alexander von Humboldt Foundation, Germany. W.M. and Z.G. gratefully acknowledge financial support from the International Science Program (ISP), Uppsala University, Sweden. K.V., W.M., and J.M. thank the Research Foundation–Flanders (FWO–Vlaanderen) for continuous financial support (project G089918N).

Conflict of Interest

The authors declare no conflict of interest.

Data Availability Statement

The data that support the findings of this study are available from the corresponding author upon reasonable request.

Keywords

high-temperature operation, organic photovoltaics, simulations

Received: July 25, 2023
Revised: October 1, 2023
Published online:

[1] a) R. Vaillon, S. Parola, C. Lamnatou, D. Chemisana, *Cell Rep. Phys. Sci.* **2020**, *1*, 100267; b) E. Skoplaki, J. A. Palyvos, *Sol. Energy* **2009**, *83*, 614; c) F. Perin Gasparin, F. Detzel Kipper, F. Schuck De Oliveira, A. Krenzinger, *Sol. Energy* **2022**, *244*, 126; d) Y.-W. Su, S.-C. Lan, K.-H. Wei, *Mater. Today* **2012**, *15*, 554.
[2] C. J. M. Emmott, D. Moia, P. Sandwell, N. Ekins-Daukes, M. Hösel, L. Lukoschek, C. Amarasinghe, F. C. Krebs, J. Nelson, *Sol. Energy Mater. Sol. Cells* **2016**, *149*, 284.
[3] K. Hasan, S. B. Yousuf, M. S. H. K. Tushar, B. K. Das, P. Das, M. S. Islam, *Energy Sci. Engineering* **2022**, *10*, 656.
[4] a) Z. Ping, F. Xie, X. Gong, L. Liu, J. Leng, Y. Liu, *Polymers* **2023**, *15*, 1893; b) R. Verduci, V. Romano, G. Brunetti, N. Yaghoobi Nia, A. Di Carlo, G. D'angelo, C. Ciminelli, *Adv. Energy Mater.* **2022**, *12*, 2200125; c) A. Bermudez-Garcia, P. Voarino, O. Raccurt, *Appl. Energy* **2021**, *290*, 116757.
[5] R. Thirsk, A. Kuipers, C. Mukai, D. Williams, *Can. Med. Assoc. J.* **2009**, *180*, 1216.
[6] M. Kaltenbrunner, M. S. White, E. D. Głowacki, T. Sekitani, T. Someya, N. S. Sariciftci, S. Bauer, *Nat. Commun.* **2012**, *3*, 770.
[7] I. Cardinaletti, T. Vangerven, S. Nagels, R. Cornelissen, D. Schreurs, J. Hruby, J. Vodnik, D. Devisscher, J. Kesters, J. D'haen, A. Franquet, V. Spampinato, T. Conard, W. Maes, W. Deferme, J. V. Manca, *Sol. Energy Mater. Sol. Cells* **2018**, *182*, 121.
[8] a) M. Corazza, F. C. Krebs, S. A. Gevorgyan, *Sol. Energy Mater. Sol. Cells* **2015**, *143*, 467; b) I. Visoly-Fisher, A. Mescheloff, M. Gabay, C. Bounioux, L. Zeiri, M. Sansotera, A. E. Goryachev, A. Braun, Y. Galagan, E. A. Katz, *Sol. Energy Mater. Sol. Cells* **2015**, *134*, 99; c) K. Burlafinger, S. Strohm, C. Joisten, M. Woiton, A. Classen, J. Hepp, T. Heumüller, C. J. Brabec, A. Vetter, *Prog. Photovoltaics* **2022**, *30*, 518.
[9] J. B. Patel, P. Tiwana, N. Seidler, G. E. Morse, O. R. Lozman, M. B. Johnston, L. M. Herz, *ACS Appl. Mater. Interfaces* **2019**, *11*, 21543.
[10] a) A. Azeez, K. S. Narayan, *J. Phys. Chem. C* **2021**, *125*, 12531; b) Y.-C. Lin, C.-H. Chen, B.-S. Tsai, T.-F. Hsueh, C.-S. Tsao, S. Tan, B. Chang, Y.-N. Chang, T.-Y. Chu, C.-E. Tsai, C.-S. Chen, Y. Yang, K.-H. Wei, *Adv. Funct. Mater.* **2023**, *33*, 2215095.
[11] a) S. Park, T. Kim, S. Yoon, C. W. Koh, H. Y. Woo, H. J. Son, *Adv. Mater.* **2020**, *32*, 2002217; b) M. Li, W. Liu, F. Zhang, X. Zhang, A. A. Abaker Omer, Z. Zhang, Y. Liu, S. Zhao, *Sol. Energy Mater. Sol. Cells* **2021**, *229*, 111103.
[12] a) H. K. H. Lee, J. R. Durrant, Z. Li, W. C. Tsoi, *J. Mater. Res.* **2018**, *33*, 1902; b) M. O. Reese, S. A. Gevorgyan, M. Jørgensen, E. Bundgaard, S. R. Kurtz, D. S. Ginley, D. C. Olson, M. T. Lloyd, P. Morvillo, E. A. Katz, A. Elschner, O. Haillant, T. R. Currier, V. Shrotriya, M. Hermenau, M. Riede, K. R. Kirov, G. Trimmel, T. Rath, O. Inganäs, F. Zhang, M. Andersson, K. Tvingstedt, M. Lira-Cantu, D. Laird, C. Mcguiness, S. (J). Gowrisanker, M. Pannone, M. Xiao, J. Hauch, et al., *Sol. Energy Mater. Sol. Cells* **2011**, *95*, 1253.
[13] a) R. F. Bailey-Salzman, B. P. Rand, S. R. Forrest, *Appl. Phys. Lett.* **2007**, *91*, 013508; b) I. Riedel, J. Parisi, V. Dyakonov, L. Lutsen, D. Vanderzande, J. C. Hummelen, *Adv. Funct. Mater.* **2004**, *14*, 38; c) K. Vandewal, K. Tvingstedt, A. Gadisa, O. Inganäs, J. V. Manca, *Phys. Rev. B* **2010**, *81*, 125204; d) D. Chirvase, Z. Chiguvare, M. Knipper, J. Parisi, V. Dyakonov, J. C. Hummelen, *J. Appl. Phys.* **2003**, *93*, 3376.
[14] E. A. Katz, D. Faiman, S. M. Tuladhar, J. M. Kroon, M. M. Wienk, T. Fromherz, F. Padinger, C. J. Brabec, N. S. Sariciftci, *J. Appl. Phys.* **2001**, *90*, 5343.
[15] a) P. Schilinsky, C. Waldauf, C. J. Brabec, *Appl. Phys. Lett.* **2002**, *81*, 3885; b) N. Bristow, J. Kettle, *J. Renew. Sustainable Energy* **2015**, *7*, 013111.
[16] D. Mühlbacher, M. Scharber, M. Morana, Z. Zhu, D. Waller, R. Gaudiana, C. Brabec, *Adv. Mater.* **2006**, *18*, 2884.
[17] D. Lee, J. Kim, G. Park, H. W. Bae, M. An, J. Y. Kim, *Polymers* **2020**, *12*, 992.
[18] a) J.-M. Jiang, H.-K. Lin, Y.-C. Lin, H.-C. Chen, S.-C. Lan, C.-K. Chang, K.-H. Wei, *Macromolecules* **2014**, *47*, 70; b) J.-M. Jiang, P. Raghunath, H.-K. Lin, Y.-C. Lin, M. C. Lin, K.-H. Wei, *Macromolecules* **2014**, *47*, 7070.
[19] a) Z. Xiao, K. Sun, J. Subbiah, T. Qin, S. Lu, B. Purushothaman, D. J. Jones, A. B. Holmes, W. W. H. Wong, *Polym. Chem.* **2015**, *6*, 2312; b) N. Zhou, A. S. Dudnik, T. I. N. G. Li, E. F. Manley, T. J. Aldrich, P. Guo, H.-C. Liao, Z. Chen, L. X. Chen, R. P. H. Chang, A. Facchetti, M. Olvera De La Cruz, T. J. Marks, *J. Am. Chem. Soc.* **2016**, *138*, 1240; c) K. D. Deshmukh, R. Matsidik, S. K. K. Prasad, L. A. Connal, A. C. Y. Liu, E. Gann, L. Thomsen, J. M. Hodgkiss, M. Sommer, C. R. Mcneill, *Adv. Funct. Mater.* **2018**, *28*, 1707185.
[20] L. Huo, T. Liu, B. Fan, Z. Zhao, X. Sun, D. Wei, M. Yu, Y. Liu, Y. Sun, *Adv. Mater.* **2015**, *27*, 6969.
[21] P. Huang, J. Du, S. S. Gunathilake, E. A. Rainbolt, J. W. Murphy, K. T. Black, D. Barrera, J. W. P. Hsu, B. E. Gnade, M. C. Stefan, M. C. Biewer, *J. Mater. Chem. A* **2015**, *3*, 6980.
[22] C. H. Peters, I. T. Sachs-Quintana, J. P. Kastrop, S. Beaupré, M. Leclerc, M. D. Mcgehee, *Adv. Energy Mater.* **2011**, *1*, 491.
[23] W. Greenbank, L. Hirsch, G. Wantz, S. Chambon, *Appl. Phys. Lett.* **2015**, *107*, 263301.
[24] D. Li, L. Song, Y. Chen, W. Huang, *Adv. Sci.* **2020**, *7*, 1901397.
[25] K. Vandewal, *Ann. Rev. Phys. Chem.* **2016**, *67*, 113.
[26] D. Bartesaghi, I. D. C. Pérez, J. Kniepert, S. Roland, M. Turbiez, D. Neher, L. J. A. Koster, *Nat. Commun.* **2015**, *6*, 7083.
[27] B. R. Paudyal, A. G. Imenes, *Sol. Energy* **2021**, *224*, 425.
[28] Z. Dong, W. Li, H. Wang, X. Jiang, H. Liu, L. Zhu, H. Chen, *Sol. RRL* **2021**, *5*, 2100370.
[29] Z. Dong, W. Li, H. Wang, X. Jiang, H. Liu, L. Zhu, H. Chen, *Matter* **2022**, *5*, 448.
[30] S. R. Raga, F. Fabregat-Santiago, *Phys. Chem. Chem. Phys.* **2013**, *15*, 2328.
[31] https://www.nrel.gov/pv/interactive-cell-efficiency.html (accessed: April 2023).
[32] Z. Yin, S. Mei, P. Gu, H.-Q. Wang, W. Song, *iScience* **2021**, *24*, 103027.
[33] L. Zhou, L. Meng, J. Zhang, C. Zhu, S. Qin, I. Angunawela, Y. Wan, H. Ade, Y. Li, *Adv. Funct. Mater.* **2022**, *32*, 2109271.
[34] J. Kettle, V. Stoichkov, D. Kumar, M. Corazza, S. A. Gevorgyan, F. C. Krebs, *Sol. Energy Mater. Sol. Cells* **2017**, *167*, 53.
[35] https://research.edm.uhasselt.be/simiconductor/web/pn.html, (accessed: January 2020).
[36] a) S. P. Tiwari, E. B. Namdas, V. Ramgopal Rao, D. Fichou, S. G. Mhaisalkar, *IEEE Electron Device Lett.* **2007**, *28*, 880; b) A. Sarkar, A. Bin Rahaman, D. Banerjee, *J. Phys. D Appl. Phys.* **2018**, *51*, 095602.
[37] M. A. Green, *J. Appl. Phys.* **1990**, *67*, 2944.
[38] a) M. N. Zidan, N. Everitt, T. Ismail, I. S. Fahim, *Polymers* **2021**, *13*, 3224; b) V. M. Le Corre, A. R. Chatri, N. Y. Doumon, L. J. A. Koster, *Adv. Energy Mater.* **2017**, *7*, 1701138; c) A. H. Fallahpour, A. Gagliardi, F. Santoni, D. Gentilini, A. Zampetti, M. Auf Der Maur, A. Di Carlo, *J. Appl. Phys.* **2014**, *116*, 184502.